Collective Ferromagnetism of Artificial Square Spin Ice

N. S. Bingham,[1] X. Zhang,[1] J. Ramberger,[2] O. Heinonen,[3,*] C. Leighton,[2] and P. Schiffer[1,4]
[1]Department of Applied Physics, Yale University, New Haven, Connecticut 06511, USA
[2]Department of Chemical Engineering and Materials Science, University of Minnesota, Minneapolis, Minnesota 55455, USA
[3]Materials Science Division, Argonne National Laboratory, Argonne, Illinois 60439, USA
[4]Department of Physics, Yale University, New Haven, Connecticut 06511, USA

(Received 9 March 2022; revised 4 May 2022; accepted 23 June 2022; published 5 August 2022)

We study the temperature and magnetic field dependence of the total magnetic moment of large-area permalloy artificial square spin ice arrays. The temperature dependence and hysteresis behavior are consistent with the coherent magnetization reversal expected in the Stoner-Wohlfarth model, with clear deviations due to interisland interactions at small lattice spacing. Through micromagnetic simulations, we explore this behavior and demonstrate that the deviations result from increasingly complex magnetization reversal at small lattice spacing, induced by interisland interactions, and depending critically on details of the island shapes. These results establish new means to tune the physical properties of artificial spin ice structures and other interacting nanomagnet systems, such as patterned magnetic media.

DOI: 10.1103/PhysRevLett.129.067201

Artificial spin ice (ASI) systems [1] consisting of two-dimensional arrays of ferromagnetic single-domain nanoislands can be studied in a nearly limitless range of lattice geometries that lead to exotic collective behavior [2–5]. Control over the design of the lattice geometry has enabled experimental study of a range of physical phenomena, including classical statistical physics models, magnetic-monopole-like excitations, and unusual topological physics [4,5], as well as possible applications, including novel computing paradigms and magnonic devices [6–8]. ASI studies typically treat the individual ferromagnetic elements as simple Ising-like moments that switch between orientations with thermal fluctuations or upon the application of a magnetic field. The reversal of island moments is recognized, however, to have considerable complexity [9–16], with dependence on island size and shape as well as the lattice spacing and geometry [10,13,17–20]. Notably, ASI also serves as an accessible model platform for probing superparamagnetism with an unusually high degree of control over the moments and their interactions [21].

Despite extensive recent attention, only a small number of researchers have examined the collective static magnetization of entire ASI arrays [20,22–31], due to the large array dimensions required. Although these prior measurements indicate that the magnetization of an array has quite different properties from the bulk constituent ferromagnetic materials, there has been little systematic attention paid to this fundamental collective property.

Here, we present a detailed experimental and simulation study of the magnetization of extended square ASI arrays, examining the temperature and field dependence of the magnetization of arrays with varied lattice spacing. We find behavior consistent with coherent magnetization reversal, closely following expectations of the Stoner-Wohlfarth model [32,33] for large lattice spacings, but with systematic deviations at small spacing. We compare our results to micromagnetic simulations, demonstrating that these deviations result from interisland interactions that depend critically on individual island shape. Our results highlight a path to a fine-tuning of the magnetic response of ASI and other nanomagnet arrays, with implications for both device applications [7,8,34,35] and novel collective magnetic states.

Our permalloy ($Ni_{0.80}Fe_{0.20}$) square ASI arrays were patterned via electron-beam lithography (Fig. 1) at thicknesses $t = 10$, 15, and 25 nm, on Si/SiO_x substrates, including two sets of $t = 25$ nm samples, labeled A and B. Each array is composed of approximately 25 million islands, with lateral array sizes of 1×1 mm^2 to 3.5×3.5 mm^2. Such large array sizes are required because of the extremely small moment of each island ($\sim 10^{-13}$ emu). For each thickness, we studied arrays with varying lattice spacing ($a = 320$, 380, 500, and 1000 nm), as well as a separate set of samples (labeled C) with $t =$ 25 nm and with $a = 280$, 290, 300, 310, 320, 340, 360, and 380 nm. These spacings correspond to distances from the end of the islands to the vertex center of 30–390 nm, for $a = 280$ and 1000 nm, respectively. The island size for all arrays was $(220 \pm 11) \times (80 \pm 8)$ nm. At these thicknesses, the Curie temperature (T_C) is at or near the bulk value (~850 K) [36]; thus, all measurements occur well below the superparamagnetic blocking temperature [37,38]. For comparison, we also measured a continuous permalloy film with $t = 25$ nm. Samples were measured in a commercial superconducting quantum interference device magnetometer (MPMS3, Quantum Design), with

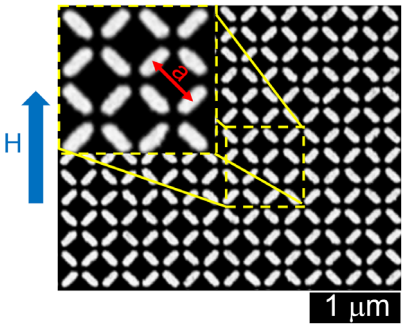

FIG. 1. Scanning electron microscope image of a portion of a $t = 25$ nm sample (sample B) with lattice spacing $a = 320$ nm. The applied magnetic field (H) direction is shown.

the magnetic field (H) aligned 45° from the long axis of the islands so that all islands have the same orientation relative to H (Fig. 1) [18,23,25].

For temperature-dependent measurements, arrays were measured on warming after field polarization at high temperature and cooling in zero field. We define the magnetization (M) as the measured magnetic moment normalized by the total number of islands. The saturation magnetization (M_S) is taken as the magnetization at +2 kOe, and the remanent magnetization (M_R) is the value at $H = 0$ upon decreasing the field from positive saturation. The coercive field (H_C) is taken as the $M = 0$ crossing point averaged over positive and negative fields (or at the maximum slope in the hysteresis loop for the small number of samples with significant background contributions at $H_C \approx 0$; see part SM-5 of the Supplemental Material [39]). We define M_S, M_R, and H_C in Fig. 2(c). The values of magnetization are typically normalized to M_S to account for lithographic defects, which introduce an uncertainty of ~10% in measured M values (see part SM-1 of the Supplemental Material [39]). Most data shown below are for $t = 25$ nm (sample B), where such effects were minimized, and our results are consistent across all sample thicknesses.

In the inset of Fig. 2(a), we show $M_R(T)$ at various lattice spacings, where small vertical offsets among the curves are attributable to lithographic defects (see part SM-1 of the Supplemental Material [39]). The temperature dependence of M_R is considerable (~10%), even in this regime well below T_C. We note that the form of $M_R(T)$ is consistent among all lattice spacings and with the continuous films, as shown in the normalized data in Fig. 2(a). This suggests that lateral dimensions of the islands and interisland interactions do not substantially impact the thermally excited spin dynamics that are responsible for the temperature dependence of M_R. While continuous permalloy films are very soft, with $H_C \approx 1$ Oe, the shape anisotropy of ASI islands leads to H_C values of several hundred oersteds [23,28,29], as shown in Figs. 2(b) and 2(c), where we illustrate the temperature evolution of H_C.

To further understand these temperature dependences, in Fig. 2(d) we plot $\Delta M(T) = [M(25\text{ K}) - M(T)]$ for both $M_R(T)$ and $M_S(T)$, as well as $\Delta H_C(T) = [H_C(25\text{ K}) - H_C(T)]$. We show these data on a log-log scale, normalized to the low-temperature values, demonstrating a clear power-law dependence. Fits for $T > 100$ K (to avoid spurious effects from sidewall oxidation [40,41]) give $\Delta H_C(T) \propto T^{1.46\pm0.03}$, $\Delta M_S(T) \propto T^{1.56\pm0.04}$, and $\Delta M_R(T) \propto T^{2.08\pm0.02}$. Importantly, the proportionality of $\Delta H_C(T)$ and $\Delta M_S(T)$ is consistent with expectations from the Stoner-Wohlfarth model for coherent rotation of the island moments [12,42], in which

$$H_C \propto \frac{K}{M_S}, \qquad K \propto M_S^2,$$

where K is the (uniaxial) shape anisotropy constant. The first proportionality here arises from the Stoner-Wohlfarth model, while the second arises from shape anisotropy, assuming (as expected in permalloy) that it is dominant over magnetocrystalline anisotropy. Our measured exponents are consistent across all measured samples and lattice spacings (see part SM-5 of the Supplemental Material [39]), and thus affirm previous evidence for coherent moment reversal in similar artificial spin ice systems [10,18].

We note that the common measured exponent for $\Delta H_C(T)$ and $\Delta M_S(T)$ is also consistent with expectations for a Bloch-like ($T^{3/2}$) dependence of the magnon-induced suppression of the magnetization in conventional ferromagnets [43]. The difference between the exponent values for $\Delta M_S(T)$ and $\Delta M_R(T)$ can be ascribed to the suppression of low-energy (long-wavelength) spin waves in an applied field, when one notes that finite dimensions are well known to affect spin waves, and thus also the temperature-dependent magnetization in nanoscale ferromagnets [44–51]. In addition, the difference between the exponent values for $M_R(T)$ and $M_S(T)$ is less dramatic in our continuous permalloy films, where we find $M_R \propto T^{1.88}$ and $M_S \propto T^{1.7}$. This again suggests that the field-suppressed spin waves in our ASI samples are those impacted by the lateral island dimensions. We note that the lowest-lying spin waves at the Γ point in the first Brillouin zone of a square ASI are edge modes formed by oscillations of the magnetization localized near island edges [9]. These modes may lie below the uniform Kittel-like mode, and, in the presence of an external field, these modes contribute less to the thermal spin excitations that suppress the magnetization at finite temperatures.

In Figs. 3(a) and 3(b), we see that $H_C(a)$ is approximately constant for $a \geq 500$ nm and then decreases at smaller spacing, which is consistent with previous measurements [23]. Figure 3(c) shows that qualitatively similar lattice-spacing dependence is observed for all thicknesses, and that H_C decreases with decreasing t, which is consistent with the expected smaller energy barrier to

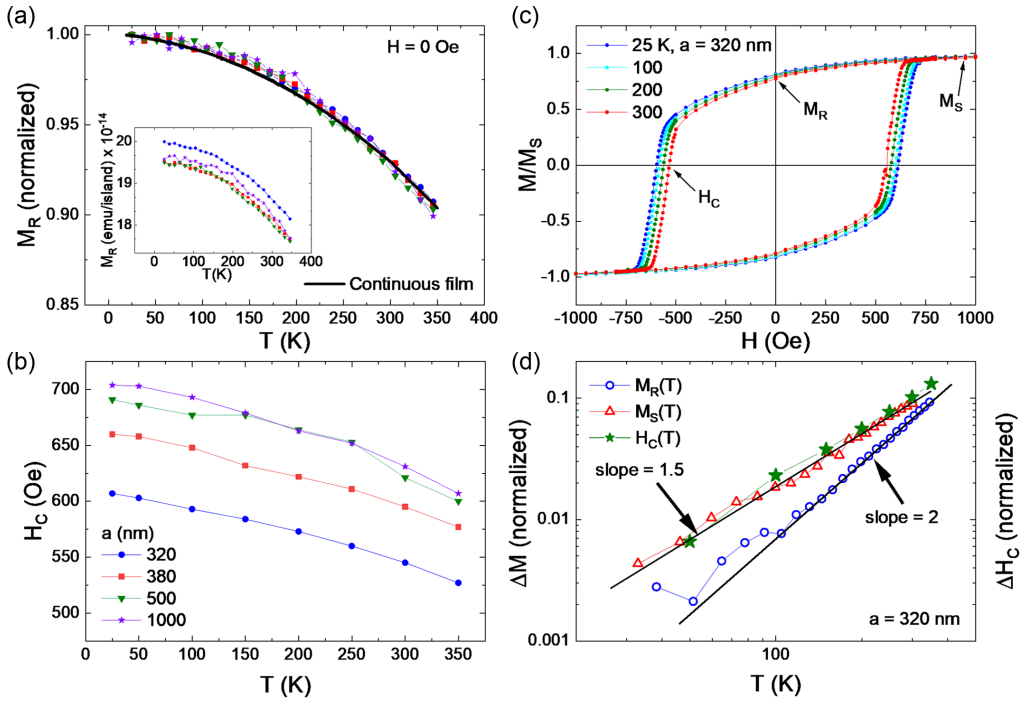

FIG. 2. (a) Remanent magnetization, $M_R(T)$, normalized to the value at $T = 25$ K for various lattice spacings and a continuous film with $t = 25$ nm after each array was field polarized at $T = 380$ K. Inset: the same $M_R(T)$ values without normalization. The legend is presented in (b). (b) $H_C(T)$ for $a = 320$, 380, 500, and 1000 nm. The small relative variation between the data for the two largest values of a is well within the measurement uncertainty. (c) $M(H)$ for a variety of temperatures for $a = 320$ nm. (d) Log-log plots of $\Delta M(T) = [M_{T=25\text{ K}} - M(T)]$ for ΔM_S and ΔM_R and $\Delta H_C(T) = [H_{C,T=25\text{ K}} - H_C(T)]$ for $a = 320$ nm, normalized to the $T = 25$ K values of M_S, M_R, and H_C, respectively. Solid lines show power laws, as described in the text. All data are for $t = 25$ nm, sample B.

magnetization reversal. The three values of t were chosen to validate the results for different moments and interaction strengths. The saturation of $H_C(a)$ at larger lattice spacing indicates that the behavior appropriately asymptotes to the case of noninteracting islands. The lattice-spacing dependence at small spacing is consistent with expectations that interactions become most important in that limit. The slope of $H_C(a)$ increases substantially for the smallest lattice spacing, as expected due to the nonlinear strength of dipolar interactions with island separation. The decrease in $H_C(a)$ continues down to our smallest measured lattice spacing of $a = 280$ nm, as shown in part SM-4 of the Supplemental Material [39] for sample C.

The shape of $M(H)$ in Fig. 3(a) provides further evidence that the magnetization reversal in this system is qualitatively consistent with expectations of Stoner-Wohlfarth in the large-spacing limit [32,33]. The expected $M(H)$ for ideal Stoner-Wohlfarth behavior is shown in Fig. 4(a) (details are given in part SM-8 of the Supplemental Material [39]), where the qualitative similarity to the shape of the experimental hysteresis loops is notable, especially for $a = 1000$ nm in Fig. 3(a). However, experimental loops become markedly more square by $a = 320$ nm, suggesting that interisland interactions induce deviations from coherent magnetization rotation, as might be expected [14,18]. These conclusions are reinforced by the behavior of M_R/M_S shown in Fig. 3(d), where this "squareness ratio" is close to $\sim 1/\sqrt{2} = 0.707$, the Stoner-Wohlfarth value, but consistently higher for $a < 380$ nm. Outliers in Fig. 3(d) (e.g., for $t = 10$ nm) are presumably associated with nonideal $M(H)$ curves with steps at small H in various samples (see parts SM-2 and SM-5 of the Supplemental Material [39]).

To better understand the magnetization reversal process, we performed athermal micromagnetic simulations (details are given in part SM-7 of the Supplemental Material [39] and in Ref. [52]). Because there are many factors that cannot be reproduced precisely in micromagnetic simulations, including edge roughness and thermal fluctuations, we used the (temperature-dependent) M_S as a fitting parameter to obtain $M(H)$ loops in good qualitative and semiquantitative agreement with the experiment. For the results shown here, we used $M_S = 700 \times 10^3$ A/m and assumed zero intrinsic magnetocrystalline anisotropy and a micromagnetic exchange parameter $A = 13$ pJ/m [53] (the effects of changing A are discussed in part SM-7 of the Supplemental Material [39]). Measurements at 300 K give $M_S = 733 \times 10^3$ A/m for continuous 25-nm-thick films, and $\sim 800 \times 10^3$ A/m for bulk permalloy [54]. We used an island thickness $t = 25$ nm and varied the lattice spacing

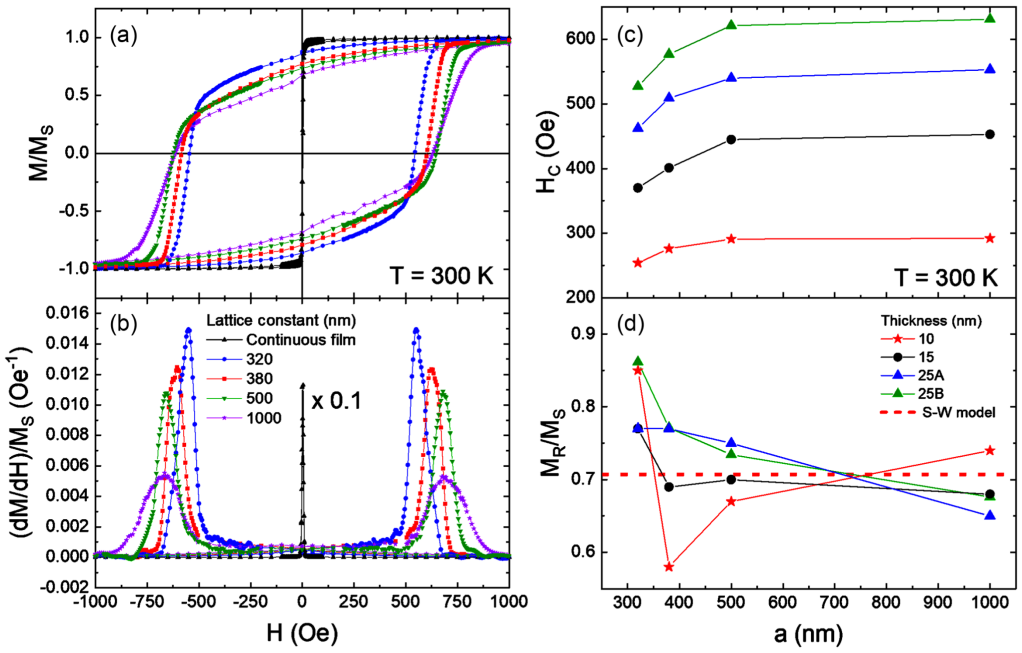

FIG. 3. (a) $M(H)$ at 300 K for $t = 25$ nm sample B for a variety of a, including the 25 nm continuous film for comparison [the legend is shown in (b)]. (b) Normalized derivative $(dM/dH)/M_S$ of the data in (a), showing broadening of the loop with increasing a (data smoothed using adjacent averaging over five neighboring points). (c) $H_C(a)$ at 300 K for multiple island thicknesses. (d) M_R/M_S at 300 K as a function of a, with the Stoner-Wohlfarth (S-W) value of 0.707 shown for comparison.

and shape. Simulated islands are oriented along the horizontal (x) and vertical (y) directions, with H applied 45° to the horizontal direction.

Previous micromagnetic simulations showed that the single island reversal process is strongly impacted by the shape of the island ends [13]. We therefore used two different island shapes in our simulations in Fig. 4(d): S1 (a rectangle with semicircular ends) and S2 (a rectangle with elliptical ends), as detailed in part SM-6 of the Supplemental Material [39]. Lithographic variations of our samples seen in SEM indicate variations of island shapes that do not perfectly map to either S1 or S2; however, simulations for both shapes give values of H_C within ~10% of the measured low-temperature value. As shown in Fig. 4(a), shape S2 generates good qualitative agreement with both experiments and the Stoner-Wohlfarth model with respect to the form of $M(H)$. However, shape S1 has qualitatively different hysteresis loops [see Fig. 4(b)] that include a sharp change in slope and small steps in the magnetization near H_C, thus confirming the sensitivity to island shape.

To develop a more quantitative understanding, we plot $\bar{m}_y$, which is the vertical component of the magnetization, $m_y(H) = M_y(H)/M_S$, for horizontal islands of shape S2 in the inset to Fig. 4(c), averaged over the full island. These data show a sharp minimum corresponding to magnetization reversal, with the depth of this minimum corresponding to how coherently the magnetization rotates. In the main panel of Fig. 4(c), we plot the depth of that minimum as a function of lattice spacing. We see that the minimum of $\bar{m}_y$ is near the expected value for the Stoner-Wohlfarth model at large spacings but rises significantly at smaller lattice spacings. This rise simply reflects that the magnetization has a more substantial twist from one edge of the island to the other during the reversal process (as seen in Fig. 5), causing the loop to be more square. This confirms that the island reversal is largely coherent in the absence of interisland interactions.

While the hysteresis loops suggest that shape S2 is a more appropriate model to capture the behavior of our system, the effects of the interisland interactions indicate that a more nuanced understanding is required [55]. Figure 5 shows a mapping of the magnetization from simulations for both island shapes S1 and S2, at fields corresponding to M_S, M_R, and H_C for $a = 280$, 320, and 1000 nm. The arrows show the local direction of the magnetization, and the color scale indicates the local value of m_y for islands aligned along the x axis. The effects of the interisland interactions are readily apparent from the spread in colors for the island near H_C, where a wider spread in colors implies less coherent rotation. Smaller lattice spacings create local fields, which impact rotation of the island magnetization near the island ends, thus making the reversal less coherent. We note that even though the magnetization rotation is not fully coherent, the magnetization texture in islands of our studied size and shape is always smooth and not broken into distinct domains, which cannot be assumed in all cases [8].

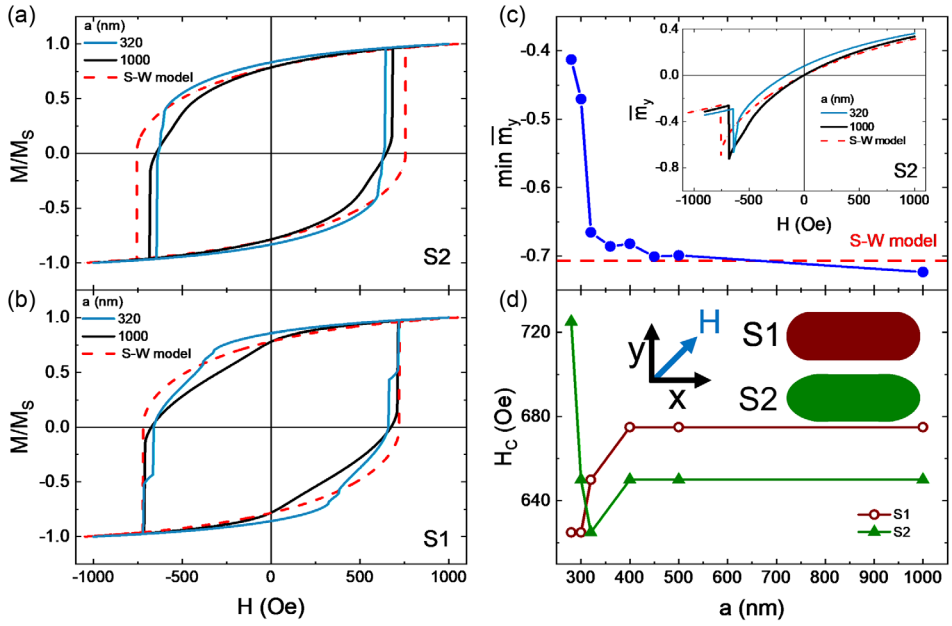

FIG. 4. Simulated $M(H)$ (averaged over all islands) for $a = 320$ and 1000 nm, and an ideal curve from the Stoner-Wohlfarth (S-W) model for (a) shape S2 and (b) shape S1. (c) The minimum value of the y component of the average magnetization ($\bar{m}_y$) of the horizontal islands as a function of magnetic field from $+1000$ to -1000 Oe with the field at 45° to the x axis. The dotted line shows the minimum value of $\bar{m}_y$ generated from the Stoner-Wohlfarth model. Inset: $\bar{m}_y(H)$ for the Stoner-Wohlfarth model and for $a = 320$ and 1000 nm for shape S2. (d) Simulated H_C as a function of lattice spacing for shapes S1 and S2 and outlines of island shapes S1 and S2, showing the different end curvature.

Since interisland interactions suppress coherence of magnetization reversal, we can now understand the reduced H_C for smaller lattice spacings as a consequence of a smaller energy barrier for a less coherent reversal process in ASI. This is the case for both shapes S1 and S2 down to $a = 320$ nm [Fig. 4(d)]. As a is reduced below 320 nm, however, the simulated $M(H)$ of the S1 and S2 arrays become markedly different, as shown in Fig. 4(d). H_C increases dramatically with further reduced lattice spacing for shape S2. By contrast, for S1, H_C decreases with further decreasing lattice spacing for $a < 320$ nm. This difference between S1 and S2 can be understood in terms of the energy cost associated with the magnetization rotating near the curved edge of the islands. For the elliptical edges of S2, there is increased energy cost to rotate the magnetization. This effect is greatly enhanced by strong interisland interactions, which couple to the more elliptical shape to create good flux closure horizontally and vertically at a vertex. Experimentally, microscopic island edge roughness presumably suppresses this energy cost, leading to behavior more like that of shape S1.

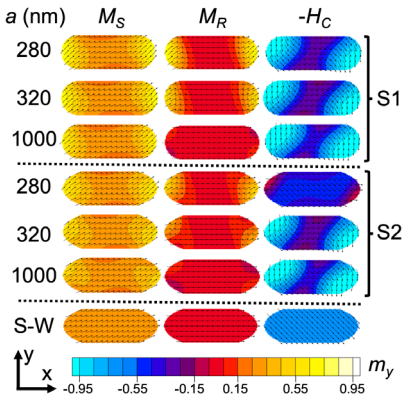

FIG. 5. Simulated magnetization maps of individual islands for $a = 280$, 320, and 1000 nm at M_S ($H = 1000$ Oe), M_R ($H = 0$), and $-H_C$ for island shapes (top) S1 ($H_C = -640$, -660, and -710 Oe for 280, 320, and 1000 nm, respectively), (middle) S2 ($H_C = -735$, -635, and -680 Oe for 280, 320, and 1000 nm, respectively), and (bottom) ideal Stoner-Wohlfarth model mapped onto shape S2 ($H_C = -514.5$ Oe). The values chosen for H_C are taken just prior to the moment reversal. Arrows indicate the local direction of the magnetization, and color coding indicates its normalized component m_y with the field applied at 45° to the horizontal direction.

The substantial temperature and lattice-spacing dependence in our measurements of M and H_C has direct implications for future studies in these systems, since fine-tuning of experimental protocols will need to take these effects into account. This is especially true for strongly interacting arrays, where the simple expectation of coherent magnetization reversal following a Stoner-Wohlfarth model begins to break down. More generally, the results also have implications for the wide range of other interacting nanomagnet systems, including a range of

superparamagnetic materials and patterned media that have important technological implications. Because the exact nature of the interaction-induced effects at low lattice spacing depend crucially on details of the shape of the islands, precise lithographic control could exploit this dependence to further control the collective behavior. This creates the possibility for new degrees of freedom in tuning the behavior of these systems, for both applications and exploration of the fundamental physics of the collective phenomena.

Lithography and experimental measurements were conducted by N. S. B., X. Z., and P. S. at Yale University and were funded by the U.S. Department of Energy, Office of Basic Energy Sciences, Materials Sciences and Engineering Division, under Grant No. DE-SC0020162. Sample growth was performed by J. R. and C. L. at the University of Minnesota and was supported by NSF through Grant No. DMR-2103711. Simulations were conducted by O. H. at Argonne National Laboratory with funding from the U.S. Department of Energy, Office of Science, Basic Energy Sciences Division of Materials Sciences and Engineering. Data analysis and manuscript preparation were performed by N. S. B., O. H., C. L., and P. S.. We gratefully acknowledge the computing resources provided on Blues, a high-performance computing cluster operated by the Laboratory Computing Resource Center at Argonne National Laboratory. We would also like to acknowledge Zhixin Zhang and Axel Hoffmann for the useful discussions and verification.

*Present and permanent address: Seagate Technology, Bloomington, Minnesota 55435, USA.

[1] R. F. Wang *et al.*, Artificial "spin ice" in a geometrically frustrated lattice of nanoscale ferromagnetic islands, Nature (London) **439**, 303 (2006).

[2] B. Canals, I.-A. Chioar, V.-D. Nguyen, M. Hehn, D. Lacour, F. Montaigne, A. Locatelli, T. O. Menteş, B. S. Burgos, and N. Rougemaille, Fragmentation of magnetism in artificial kagome dipolar spin ice, Nat. Commun. **7**, 11446 (2016).

[3] C. Nisoli, V. Kapaklis, and P. Schiffer, Deliberate exotic magnetism via frustration and topology, Nat. Phys. **13**, 200 (2017).

[4] S. H. Skjærvø, C. H. Marrows, R. L. Stamps, and L. J. Heyderman, Advances in artificial spin ice, Nat. Rev. Phys. **2**, 13 (2020).

[5] P. Schiffer and C. Nisoli, Artificial spin ice: Paths forward, Appl. Phys. Lett. **118**, 110501 (2021).

[6] J. S. Woods *et al.*, Switchable X-Ray Orbital Angular Momentum from an Artificial Spin Ice, Phys. Rev. Lett. **126**, 117201 (2021).

[7] H. Arava, P. M. Derlet, J. Vijayakumar, J. Cui, N. S. Bingham, A. Kleibert, and L. J. Heyderman, Computational logic with square rings of nanomagnets, Nanotechnology **29**, 265205 (2018).

[8] J. C. Gartside, K. D. Stenning, A. Vanstone, T. Dion, H. H. Holder, D. M. Arroo, F. Caravelli, H. Kurebayashi, and W. R. Branford, Reconfigurable training and reservoir computing in an artificial spin-vortex ice via spin-wave fingerprinting, Nat. Nanotechnol. **17**, 460 (2022).

[9] S. Gliga, A. Kakay, L. J. Heyderman, R. Hertel, and O. G. Heinonen, Broken vertex symmetry and finite zero-point entropy in the artificial square ice ground state, Phys. Rev. B **92**, 060413 (2015).

[10] F. Carace, P. Vavassori, G. Gubbiotti, S. Tacchi, M. Madami, G. Carlotti, and T. Okuno, Magnetization reversal process in elliptical permalloy nanodots, Thin Solid Films **515**, 727 (2006).

[11] G. M. Wysin, W. A. Moura-Melo, L. A. S. Mol, and A. R. Pereira, Magnetic anisotropy of elongated thin ferromagnetic nano-islands for artificial spin ice arrays, J. Phys. Condens. Matter **24**, 296001 (2012).

[12] G. W. Paterson, G. M. Macauley, and R. Macêdo, Field-driven reversal models in artificial spin ice, Adv. Theory Simul. **4**, 2100109 (2021).

[13] J. Li *et al.*, Tailoring magnetization reversal of a single-domain bar nanomagnet via its end geometry, AIP Adv. **11**, 045010 (2021).

[14] M. Wyss, S. Gliga, D. Vasyukov, L. Ceccarelli, G. Romagnoli, J. Cui, A. Kleibert, R. L. Stamps, and M. Poggio, Stray-field imaging of a chiral artificial spin ice during magnetization reversal, ACS Nano **13**, 13910 (2019).

[15] E. Iacocca, S. Gliga, R. L. Stamps, and O. Heinonen, Reconfigurable wave band structure of an artificial square ice, Phys. Rev. B **93**, 134420 (2016).

[16] M. Ferreira Velo, B. Malvezzi Cecchi, and K. R. Pirota, Micromagnetic simulations of magnetization reversal in kagome artificial spin ice, Phys. Rev. B **102**, 224420 (2020).

[17] S. Gliga *et al.*, Emergent dynamic chirality in a thermally driven artificial spin ratchet, Nat. Mater. **16**, 1106 (2017).

[18] N. Leo *et al.*, Chiral switching and dynamic barrier reductions in artificial square ice, New J. Phys. **23**, 033024 (2021).

[19] E. Mengotti, L. J. Heyderman, A. F. Rodriguez, F. Nolting, R. V. Hugli, and H. B. Braun, Real-space observation of emergent magnetic monopoles and associated Dirac strings in artificial kagome spin ice, Nat. Phys. **7**, 68 (2011).

[20] A. Talapatra, N. Singh, and A. O. Adeyeye, Magnetic Tunability of Permalloy Artificial Spin Ice Structures, Phys. Rev. Applied **13**, 014034 (2020).

[21] M. Pohlit *et al.* Collective magnetic dynamics in artificial spin ice probed by ac susceptibility, Phys. Rev. B **101**, 134404 (2020).

[22] X. Zhou, G.-L. Chua, N. Singh, and A. O. Adeyeye, Large area artificial spin ice and anti-spin ice $Ni_{80}Fe_{20}$ structures: Static and dynamic behavior, Adv. Funct. Mater. **26**, 1437 (2016).

[23] K. K. Kohli, A. L. Balk, J. Li, S. Zhang, I. Gilbert, P. E. Lammert, V. H. Crespi, P. Schiffer, and N. Samarth, Magneto-optical Kerr effect studies of square artificial spin ice, Phys. Rev. B **84**, 180412 (2011).

[24] V. S. Bhat, J. Sklenar, B. Farmer, J. Woods, J. T. Hastings, S. J. Lee, J. B. Ketterson, and L. E. De Long, Controlled Magnetic Reversal in Permalloy Films Patterned into Artificial Quasicrystals, Phys. Rev. Lett. **111**, 077201 (2013).

[25] N. S. Bingham *et al.*, Experimental Realization of the 1D Random Field Ising Model, Phys. Rev. Lett. **127**, 207203 (2021).

[26] S. Zhang *et al.* Perpendicular Magnetization and Generic Realization of the Ising Model in Artificial Spin Ice, Phys. Rev. Lett. **109**, 087201 (2012).
[27] O. Sendetskyi, V. Scagnoli, N. Leo, L. Anghinolfi, A. Alberca, J. Lüning, U. Staub, P. M. Derlet, and L. J. Heyderman, Continuous magnetic phase transition in artificial square ice, Phys. Rev. B **99**, 214430 (2019).
[28] T. Dion, D. M. Arroo, K. Yamanoi, T. Kimura, J. C. Gartside, L. F. Cohen, H. Kurebayashi, and W. R. Branford, Tunable magnetization dynamics in artificial spin ice via shape anisotropy modification, Phys. Rev. B **100**, 054433 (2019).
[29] S. A. Morley *et al.*, Temperature and magnetic-field driven dynamics in artificial magnetic square ice, in *Spintronics VIII*, SPIE Proceedings Vol. 9551 (SPIE—International Society for Optical Engineering, Bellingham, WA, 2015), pp. 69–80.
[30] V. Kapaklis, U. B. Arnalds, A. Harman-Clarke, E. T. Papaioannou, M. Karimipour, P. Korelis, A. Taroni, P. C. W. Holdsworth, S. T. Bramwell, and B. Hjörvarsson, Melting artificial spin ice, New J. Phys. **14**, 035009 (2012).
[31] M. Saccone, F. Caravelli, K. Hofhuis, S. Parchenko, Y. A. Birkhölzer, S. Dhuey, A. Kleibert, S. van Dijken, C. Nisoli, and A. Farhan, Direct observation of a dynamical glass transition in a nanomagnetic artificial hopfield network, Nat. Phys. **18**, 517 (2022).
[32] E. C. Stoner and E. P. Wohlfarth, A mechanism of magnetic hysteresis in heterogeneous alloys, Phil. Trans. R. Soc. London **240**, 599 (1948).
[33] C. Tannous and J. Gieraltowski, The Stoner-Wohlfarth model of ferromagnetism, Eur. J. Phys. **29**, 475 (2008).
[34] A. V. Chumak *et al.*, Advances in magnetics roadmap on spin-wave computing, IEEE Trans. Magnet. **58**, 0800172 (2022)..
[35] J. Grollier, D. Querlioz, K. Y. Camsari, K. Everschor-Sitte, S. Fukami, and M. D. Stiles, Neuromorphic spintronics, Nat. Electron. Rev. **3**, 360 (2020).
[36] X. Zhang, Y. Y. Lao, J. Sklenar, N. S. Bingham, J. T. Batley, J. D. Watts, C. Nisoli, C. Leighton, and P. Schiffer, Understanding thermal annealing of artificial spin ice, APL Mater. **7**, 111112 (2019).
[37] O. Petracic, Superparamagnetic nanoparticle ensembles, Superlattices Microstruct. **47**, 569 (2010).
[38] G. Y. Velez and A. Encinas, Superparamagnetic relaxation in interacting magnetic particle assemblies, J. Supercond. Novel Magn. **32**, 2259 (2019).
[39] See Supplemental Material at http://link.aps.org/supplemental/10.1103/PhysRevLett.129.067201 for additional data, and more details regarding simulations and experimental techniques.
[40] S. A. Morley, D. A. Venero, J. M. Porro, S. T. Riley, A. Stein, P. Steadman, R. L. Stamps, S. Langridge, and C. H. Marrows, Vogel-Fulcher-Tammann freezing of a thermally fluctuating artificial spin ice probed by x-ray photon correlation spectroscopy, Phys. Rev. B **95**, 104422 (2017).
[41] O. Ozatay *et al.*, Sidewall oxide effects on spin-torque- and magnetic-field-induced reversal characteristics of thin-film nanomagnets, Nat. Mater. **7**, 567 (2008).
[42] R. C. O'Handley, *Modern Magnetic Materials: Principles and Applications* (Wiley, New York, 1999).
[43] F. Bloch, Zur theorie des ferromagnetismus, Z. Phys. **61**, 206 (1930).
[44] C. A. F. Vaz, J. A. C. Bland, and G. Lauhoff, Magnetism in ultrathin film structures, Rep. Prog. Phys. **71**, 056501 (2008).
[45] R. Weber and P. E. Tannenwald, Long-range exchange interactions from spin-wave resonance, Phys. Rev. **140**, A498 (1965).
[46] J. Merikoski, J. Timonen, M. Manninen, and P. Jena, Ferromagnetism in Small Clusters, Phys. Rev. Lett. **66**, 938 (1991).
[47] P. V. Hendriksen, S. Linderoth, and P.-A. Lindgård, Finite-size effects in the magnetic properties of ferromagnetic clusters, J. Magn. Magn. Mater. **104–107**, 1577 (1992).
[48] P. Crespo, J. M. González, A. Hernando, and F. J. Yndurain, Spin-wave excitations in ribbon-shaped Fe nanoparticles, Phys. Rev. B **69**, 012403 (2004).
[49] U. Köbler and R. Schreiber, Exploring the 2D to 3D dimensionality crossover in thin iron films, J. Magn. Magn. Mater. **300**, 519 (2006).
[50] Y. Li, G. Gubbiotti, F. Casoli, S. A. Morley, F. J. T. Gonçalves, M. C. Rosamond, E. H. Linfield, C. H. Marrows, S. McVitie, and R. L. Stamps, Thickness dependence of spin wave excitations in an artificial square spin ice-like geometry, J. Appl. Phys. **121**, 103903 (2017).
[51] T. Dion, J. C. Gartside, A. Vanstone, K. D. Stenning, D. M. Arroo, H. Kurebayashi, and W. R. Branford, Observation and control of collective spin-wave mode hybridization in chevron arrays and in square, staircase, and brickwork artificial spin ices, Phys. Rev. Research **4**, 013107 (2022).
[52] D. K. Schreiber, O. G. Heinonen, and A. K. Petford-Long, Micromagnetic modeling of the magnetization dynamics in a circularly exchange-biased and exchange-coupled ferromagnetic multilayer, Phys. Rev. B **80**, 014411 (2009).
[53] S. Gliga, A. Kákay, R. Hertel, and O. G. Heinonen, Spectral Analysis of Topological Defects in an Artificial Spin-Ice Lattice, Phys. Rev. Lett. **110**, 117205 (2013).
[54] R. M. Bozorth, *Ferromagnetism* (IEEE Press, New York, 1993).
[55] A. Vanstone, J. C. Gartside, K. S. Stenning, T. Dion, D. M. Arroo, and W. R. Branford, Spectral fingerprinting: Microstate readout via remanence ferromagnetic resonance in artificial spin ice, New J. Phys. **24**, 043017 (2022).